The Use of Crustal Higher Modes to Constrain Crustal Structure Across Central Asia

A. L. Levshin, M. H. Ritzwoller, and N. M. Shapiro

Department of Physics, University of Colorado at Boulder, Boulder, CO 80309.

Summary

We investigate the feasibility of observing crustal higher mode surface wave dispersion and applying these observations to improve estimates of crustal structure. Because crustal overtones propagate most efficiently and are excited best in regions with thick crust and deep crustal seismicity, the study concentrates on Central and Southern Asia and parts of the Middle East. We developed a new data set of observations of the group velocities of Rayleigh and Love wave first crustal overtones between 7 sec to 18 sec period across the studied region, and present dispersion maps for the first crustal overtone between periods of 10 sec and 17 sec. Monte Carlo inversion of first higher-mode together with fundamental mode dispersion at several locations demonstrates that the higher modes significantly reduce the range of acceptable crustal models and improve the vertical resolution of the crust from the mantle. Further development of the higher-mode data set will permit a general 3-D simultaneous inversion for shear velocity structure of the crust and upper mantle in this region with better vertical resolution than in existing models (e.g., Shapiro and Ritzwoller, 2002). General application of the method across continents world-wide is probably not feasible, due to the low likelihood of observing large numbers of first overtones in regions of normal continental crustal thickness devoid of deep crustal seismicity.

Submitted to *Geophys. J. Int.*, April 23, 2004.

1. Introduction

Surface wave observations are commonly used to study crustal and upper mantle structures on local, regional and global scales. Tomographic inversions of surface wave travel times for two-dimensional (2-D) group and phase speed maps and three-dimensional (3-D) shear velocity structures are the subjects of numerous studies (e.g., Trampert & Woodhouse, 1995; Ekström et al., 1997; Shapiro & Ritzwoller, 2002; and many others). Central Asia has been a particular focus for these studies (e.g., Bourjot & Romanowicz, 1992; Wu & Levshin, 1994; Curtis & Woodhouse, 1997; Wu et al., 1997; Ritzwoller & Levshin, 1998; Ritzwoller et al., 1998; Griot et al., 1998; Huang et al., 2003; Shapiro et al., 2004), as it presents a mosaic of tectonic structures that result from the complex deformation history of the region. Because crustal structure is so varied across Central Asia, the ability to resolve the structure of the crust from the mantle is particularly problematic.

There are a number of approaches to surface wave tomography used in previous studies. Most are based on extracting dispersion information for fundamental Rayleigh and Love waves for a set of periods usually followed by a series of one-dimensional (1-D) inversions on a grid of locations for crustal and upper mantle shear velocities (e.g., Shapiro & Ritzwoller, 2002). Some authors (van Heijst & Woodhouse, 1999; Yoshizawa & Kennett, 2002) have also used higher mode phase velocities obtained by stripping these modes from the observed records. Another approach is based on full waveform fitting using synthetic seismograms for 1-D structures between source and receiver, and interpolating the estimated cross-sections to produce a 3-D model of the region of study (Nolet, 1978, 1987; Lebedev & Nolet, 2003; Friederich, 2003). Both of these approaches to introduce overtones into the inversion are applied at periods above 30 s where the overtones dominantly constrain mantle structure. The use of mantle overtones does not particularly help to improve estimates of crustal structure or to resolve the crust from the mantle. Crustal overtones at periods below 15-20 s, however, present information about crustal structure, that, if used together with fundamental mode data, may significantly improve estimates of the structure of the crust and resolution from the underlying mantle.

There have been several studies that demonstrated the observability and usefulness of crustal higher modes (e.g., Oliver & Ewing, 1957, 1958; Oliver et al., 1959; Oliver, 1962; Alexander, 1962; Brune & Dorman, 1963, Kovach and Anderson, 1964; Crampin, 1964, 1966a, 1966b; Crampin & King, 1977; Nolet, 1975, 1977). For the most part, these studies have been confined to the interpretation of a small number of particular paths. To our knowledge, there has been no attempt to use crustal higher modes in tomographic inversions. Higher mode data have also been used in a completely different frequency range (2 - 15 Hz) to study the shear velocity structure of sediments in the top few tens of meters beneath the surface and the sea floor (e.g., Gabriels et al., 1987; Ritzwoller & Levshin, 2002).

In this study we investigate the feasibility of introducing crustal overtone measurements to improve estimates of crustal structure within the context of a tomographic inversion. In section 2, we present a discussion of the physical characteristics, structural sensitivity, and excitation of crustal higher modes. We show that higher modes are expected to be best observed in regions with thick crust and with significant seismicity beneath the shallow crust. Based on these results, we have concentrated observational efforts on Central Asia and, as discussed in section 3, constructed a new data set of observations of the dispersion of the first crustal overtone between about 7 sec and 18 sec period for about 500 paths in Central Asia. In sections 4 and 5, we show first-overtone group velocity maps for Rayleigh and Love waves from 10 sec to 17 sec period and demonstrate the effect of including this information on the estimated shear velocity structure of the crust and uppermost mantle.

2. Physical background

In this section we will briefly discuss the nature of crustal higher modes and their basic properties: expected dispersion, attenuation, amplitude spectra, excitation and radiation patterns as functions of source parameters. These results form the basis for our concentration on observing the first higher-modes across Central Asia.

2.1 The nature of crustal higher modes

Crustal higher modes result from the constructive interference of overcritical multiply reflected shear waves in the Earth's crust. The simplest reflection scheme is shown in Figure 1, where a one-layered homogeneous crust of thickness H with longitudinal and shear velocities Vp_1 and Vs_1 is underlain by a homogeneous half-space with velocities Vp_2 and Vs_2 ($Vp_1 > Vs_2 > Vs_1$). The reflection angle is always above the critical value $i_{\text{crit}} = \sin^{-1}(Vs_1/Vs_2)$, and both SH and SV waves are multiply reflected from the surface and the internal interface. This explanation of the generation of higher modes is confirmed by comparing the phase velocity curves obtained by solving the full eigenvalue problems for Love and Rayleigh waves (Woodhouse, 1988) with the equations obtained from the condition of constructive interference for multiply reflected shear waves (e.g., Ewing et al., 1957; Officer, 1958):

$$\frac{2H\cos i}{Vs_1} + \frac{T\arg(R_{SH}(i))}{2\pi} = nT \quad (n = 0, 1, 2, ..) \tag{1}$$

for Love waves, and

$$\frac{2H\cos i}{Vs_1} + \frac{T[\arg(R_{SV}(i)) + \arg(R0_{SV}(i))]}{2\pi} = nT \quad (n = 1, 2, ..) \tag{2}$$

for Rayleigh waves. Here i is the angle of incidence, $i = \sin^{-1}(Vs_1/C_n(T))$, $C_n(T)$ is the phase velocity for the nth mode at period T, R_{SH} and R_{SV} are the complex reflection coefficients of the corresponding waves from the internal interface, $R0_{SV}$ is the complex reflection coefficient for the SV wave from the free surface, and arg is a function that denotes the phase of a complex number. Note that $|R_{SV}| = |R0_{SV}| = |R_{SH}| = 1$. For this simple model, the techniques provides the same results for all modes except the fundamental Rayleigh mode ($n = 0$) whose phase velocity cannot be found from equation (2) because this mode includes the boundary Rayleigh wave which exists even in a homogeneous half-space.

In reality, the structure of the crust and upper mantle is more complicated than in this simple example, and the equations above do not describe the details of wave behavior. However, the presence of a strong velocity contrast at the Moho discontinuity, with inequalities

$Vp_{cr} > Vs_M > Vs_{cr}$, where Vp_{cr} and Vs_{cr} characterize average velocities in the crust, and Vs_M is the shear velocity directly beneath the Moho, implies that this interpretation of the nature of crustal higher modes is reasonable on average. From equations (1) and (2), it is evident that crustal thickness and crustal and uppermost mantle shear velocities are the principal factors that determine the behavior of the higher mode dispersion curves.

2.2 Dispersion of higher crustal modes

To illustrate the influence of crustal structure on the dispersion of crustal higher modes for different structural and tectonic provinces, we use one-dimensional vertical profiles from a 3-D seismic model (Shapiro & Ritzwoller, 2002) at selected locations. The selected shear-velocity profiles are presented in Figure 2. Group velocity curves for Rayleigh and Love waves for the fundamental mode and the first several overtones are presented in Figure 3. Note that the second and higher overtone speeds for Rayleigh and Love waves are similar and are, therefore, hard to separate and measure directly. Parts of the fundamental and first overtone modes, however, are well separated from other modes and are measurable. This is the reason we concentrate in this paper on observations of the first Rayleigh and Love crustal overtones in addition to the fundamental modes.

Further inspection of Figure 3 reveals that at short periods (< 5 sec), the group velocity of the Love modes and the Rayleigh modes with the exception of the fundamental mode asymptotically approach the minimum shear speed in the crust. (In fact, phase and group speeds are the same in the high frequency limit.) At this location in Kazakhstan, the model of Shapiro & Ritzwoller (2002) has no sediments and that speed is about 3.6 km/sec, the shear speed of the uppermost part of the crystalline crust. At longer periods, the Rayleigh and Love overtones superpose to form a guided whispering gallery wave in the uppermost mantle, directly beneath the Moho. The period band of sensitivity to crustal thickness and shear speeds in the body of the crust is represented by the part of the dispersion curves with a large slope (between the uppermost crustal modes and mantle whispering gallery modes). This part of the first overtone branch occurs between the Airy phase between about 5-10 sec

period and about 18 sec period for Rayleigh waves and from about 10 sec to 15 sec period for Love waves. The exact period range will depend on the local structure, as the details of dispersion will vary from place to place. This is illustrated in Figure 4 which shows phase and group velocity curves from about 4 sec to 25 sec period for the four models at the locations in Figure 2. Note, in particular, how the period of the Airy phase seen in the group velocity of the first higher Rayleigh mode shifts to longer periods for the regions with thicker crust. In regions of thick crusts, the first higher mode dispersion curve is stretched horizontally to longer periods relative to regions with thinner crust. This is a fundamental observable that we will use later in the paper to constrain crustal properties.

Sensitivity kernels for phase and group velocities to perturbations in shear velocity as a function of depth at periods between 7 sec and 15 sec for the Tibetan plateau (Fig. 2) are shown in Figure 5. The maximum sensitivity at these periods is in the middle crust, at depths between 20 and 60 km for Tibet. For shield areas, maximum sensitivity is between 10 to 40 km. Sensitivity deepens as period increases. The group velocity sensitivity kernels usually have two lobes: a positive lobe in the upper crust and a negative lobe in the lower crust. The sensitivity kernels for phase velocity have only a positive lobe. Group velocity maxima are usually 1.5 to 2.0 times larger in magnitude than the maxima for the phase velocity kernels.

2.3 Amplitudes: modal Q and excitation of higher modes

The observability of the first overtone will depend on its absolute amplitude, and its amplitude relative to the fundamental mode. Its absolute amplitude depends in part on its modal quality factor, Q^*, which we show here increases with crustal thickness. We also show that its amplitude, both in absolute and relative terms, improves with deeper events.

The attenuation of higher modes is described by the modal Q value, $Q^*(T)$, which depends on the intrinsic Q profile of the crust and uppermost mantle and the depth of penetration of the modal eigenfunctions. Figure 6 illustrates how crustal thickness changes Q^*, by plotting $Q^*(T)$ for the first overtone and the fundamental modes at a location in Kazakhstan (typical

continental crustal thickness) and Tibet (exceptionally thick crust). The intrinsic Q of the crust in both cases is 600 and Q decreases in the mantle. The values of Q^* between 10 and 15 sec period for the first higher modes are significantly lower than Q^* for fundamental modes at these periods and are close to the values of Q^* for fundamental modes between 25 and 35 sec period. This is one of the reasons why the first overtones are hard to observe, they tend to be obscured by the fundamentals even though they do not directly overlap on the frequency - time diagram. Also, note that Q^* is larger for Tibet than for the Kazakh Platform starting at about 10 sec period. This is due to Tibet's thicker crust which prevents penetration of short period waves into the upper mantle with its lower Q values.

The efficiency of excitation of higher modes depends on the depth of the source, the source mechanism, and crustal structure. Although the absolute values of the reflection coefficients for shear waves at the Moho and the free surface are equal to unity, the shear velocity contrast at Moho influences the resulting amplitudes of higher modes as it determines the loss of energy leaked into the mantle. The resulting amplitudes of the higher modes will depend on several factors, including the structure of the medium and the depth and mechanism of the source (Levshin et al., 1972b; Levshin et al., 1989). The radiation pattern of the higher modes is often quite different from that for fundamental modes (Figure 7). Examples of radiation patterns for an event on 03/28/1999 in Southern Tibet are shown in Figure 7 for different source depths. The radiation pattern for the fundamental mode between 8 and 16 sec period has only two lobes, while the radiation pattern for the first higher Rayleigh mode has four lobes for source depth less than 50 km. Similar results are obtained for other source mechanisms and crustal models. The additional nodes in the overtone radiation pattern contributes to the lower chance of its observation relative to fundamental modes.

Examples of spectral amplitudes as a function of source depth for fundamental and first higher Rayleigh modes at different periods are presented in Figure 8. The source mechanism is for the same event in Southern Tibet used to construct Figure 7. Two structural models, namely, for the Tibetan Plateau and for the Kazakh Platform are selected (see Figure 2). Higher modes have significantly smaller amplitudes for shallow events, but their amplitudes

grow quickly as the source deepens. This is especially true for the Tibetan structure with the thick crust. The excitation of the higher mode at the same period is more efficient in a model with thick crust. The relative increase in intensity of the higher Rayleigh modes with increasing source depth is well observed on synthetic seismograms for the fundamental and first higher Rayleigh modes for the Tibetan model (Figure 9). For shallow events, the fundamental mode obscures the overtone. With events at 30 km depth or deeper, the amplitude of the first crustal Rayleigh overtone is commensurate with the fundamental mode amplitude, at least for the Tibetan structure. This source depth dependence is different for Love waves, however.

2.4 Summary: Expected observability of higher modes

In summary, we expect that the first overtone between about 8 sec and 18 sec period will be the best target for observation and will have the greatest relevance to crustal structure and thickness. The exact period band will depend on local structure. These waves are well separated from other interfering waves. The amplitude of the first overtone is expected to be largest in regions with thick crust and following earthquakes that are deeper than the shallow crust. Central Asia is anideal location to search for these observations, as crust is thick and seismicity deeper than the shallow crust is relatively plentiful.

3. Observations

For the reasons discussed in section 2, we limit observations to the Central Asian region extending between $10^\circ - 50^\circ$N and $40^\circ - 120^\circ$E. Concentration is on obtaining group velocity dispersion curves for the first crustal overtone starting at about 5 sec period and extending to about 20 sec. We used broad-band waveforms following earthquakes that occurred between 1977 and 2002 in and around Eurasia recorded at stations from both global networks (GDSN, GSN, GEOSCOPE) as well as temporary regional arrays (e.g., KNET, KAZNET, Saudi Arabian Network, PASSCAL deployments in Tibet and Nepal).

To identify higher modes we used the same FTAN technique that has been used previ-

ously for detecting and measuring the dispersion of fundamental modes (e.g., Levshin et al., 1972a, 1989, 1992; Ritzwoller & Levshin, 1998). Higher mode group velocity curves from FTAN diagrams were obtained only when a distinct short-period higher-mode signal was visible (e.g., Figures 10, 11). The percent of such records relative to records with distinct fundamental mode signals is small, on the order of 3%. Outliers were rejected by comparison with values obtained by ray-tracing through the group velocity maps obtained from the model of Shapiro & Ritzwoller (2002). The number of individual dispersion curves that withstood outlier rejection is shown in Figure 12. The maximum is at periods between about 8 and 15 sec. Figure 13 illustrates the coverage of the region for both Rayleigh and Love first overtones. Coverage is best in Western China, but at the shorter periods extends into Iran in the west, north into Mongolia and Kazakhstan, and east into eastern China. At the longer periods, good path coverage is exclusive to Western China and environs. This is because by 17 sec period, for example, the first higher mode in regions with thinner crust than Tibet strongly samples the mantle and is effectively unobservable. The first crustal overtone constraint on crustal structure, therefore, is a broader band and stronger constraint on the Tibetan crust than on the crust in other regions.

4. Dispersion Tomography for the First Higher Crustal Mode

Only data at periods between 10 and 17 sec were used to produce the Rayleigh and Love wave dispersion maps. The inversion technique, described by Barmin et al. (2001), was modified to account for the spatially extended frequency-dependent sensitivity of the waves as discussed by Ritzwoller et al. (2002). The use of extended sensitivity kernels has a minimal effect on the estimated maps at these periods, but provides a more accurate estimate of spatial resolution. Spatial resolution is best where data density maximizes (Fig. 13), optimizing at about 500 to 600 km in the region of study. (Resolution is estimated with the method described by Barmin et al., 2001, and is equal the standard deviation of a Gaussian fit to the resolution surface at each location.) The spatial resolution for fundamental modes between 30 sec and 40 sec period where they are most sensitive to the crust is about 250 to

300 km in this region.

Because of the highly variable data distribution, each map is estimated relative to an input reference map. The inversion is constrained to remain near the input map in regions with low path density. We used the group velocity maps for the first higher modes predicted from the 3-D model of Shapiro & Ritzwoller (2002). This highlights areas where the 3-D model needs improvement in the crust. Misfit statistics for both the input reference maps and the estimated maps are listed in Table 1. The rms-residual for the reference map is typically 25 - 35 sec, depending on period and wave type. The residual is larger for Love than Rayleigh waves, probably because the Love waves are more sensitive to the upper crust which is poorly known in the reference model. After the inversion, the rms-residuals reduce to values between 18 and 20 sec. Love wave measurements are fit as well as the Rayleigh wave measurements. Because the input reference model fits the Rayleigh overtones measurements better than the Love measurements, the variance reduction is higher for the Love waves, averaging about 60%, whereas the variance reduction for the Rayleigh waves averages about 50%. In both cases, the estimated dispersion maps fit the data much better than the input model. The measurements contain significant, new information about crustal structure.

The estimated dispersion maps for Ralyeigh and Love waves at various periods are shown in Figure 14. Figure 15 shows the difference between the estimated map and each input reference map. Comparison between Figures 13 and 15 illustrates that a perturbation in the reference structure is introduced only when there are several paths crossing a $2^\circ \times 2^\circ$ cell. The path density constraint applied here is much weaker than that in our fundamental mode inversions where we require more than 50 paths to intersect a $2^\circ \times 2^\circ$ cell before a perturbation to the underlying structure is introduced. Inspection of Figure 15 reveals that most of the perturbations are negative; that is, the observed waves travel slower than those predicted by the reference 3-D model in most regions and at most periods. The largest negative perturbations are about -400 m/s, which is about a 10% perturbation in group velocity.

Figure 14 shows that the spatial variability within each of the maps is considerably larger

than ±10%. Thus, the input 3-D model proscribes the overall pattern of anomalies expected for the first crustal overtones, but we expect that crustal velocities in the model are, on average, too high and crustal thicknesses in some cases are too small. The inversions in section 5 explore this further. To a fairly good approximation, the patterns of anomalies seen in the continental parts of Figure 14 result from crustal thickness variations in which the thicker crust manifests as low first crustal mode speeds. Tectonically deformed regions have, on average, thicker crust and hence lower crustal overtone speeds relative to adjacent non-tectonic continental crust. Low speeds at short periods in the Caspian and Arabian Seas and the Bay of Bengal result from thick sediments in the model and are largely unconstrained observationally.

5. Example Inversions for Crustal Structure

To investigate the information contained in the crustal overtone maps we performed simultaneous inversions of the overtone and fundamental mode maps at two geographical locations that have relatively good coverage by higher modes: the Northern Tien-Shan region (42°N, 74°E) and South-Western China within Tibet (30°N, 100°E). The observed dispersion curves for these two locations are shown as the solid (Rayleigh) and dashed (Love) black lines in the left panels of Figures 16 and 17. There are four observed fundamental mode curves: Rayleigh and Love group (U_0) and phase (C_0) speed. The fundamental mode measurements extend from 16 sec period up to 200 sec period for the Rayleigh wave group speed. There are two observed first overtone curves (U_1) that extend from 10 sec to 17 sec period.

The inversions are based on the Monte-Carlo method of Shapiro and Ritzwoller (2002) in which the data are the dispersion curves taken from the dispersion maps at each specified location. Fourteen model parameters describe the crust and upper mantle including the thickness as well as the shear and compressional velocities in each layer of a three-layered crust. The model is isotropic in the crust (although Shapiro et al., 2004 argue that parts of the Tibetan crust is radially anisotropic), but is radially anisotropic in the mantle to a depth of about 200 km and structural perturbations are continuous, being represented by

B-splines. Results of the inversion for the two chosen locations are shown in Figures 16 and 17 (right panels). At each depth the full range of models is displayed, defining a corridor of allowed models. The isotropic part of the model in the mantle is shown by taking the average of the V_{sv} and V_{sh} components at each depth and displaying the range of the results. The top pair of panels in each figure shows the inversion without the higher-mode constraint, but shows how the higher mode would be fit if the inversion is constrained only by fundamental mode data. The bottom pair of panels in each figure shows the inversion and fit to all data from the inversion that fits the higher-mode and fundamental mode data simultaneously.

Figures 16a and 17a demonstrate that without the overtone data in the inversion, the overtone data are poorly fit and the range of models in the crust is large. Including the overtone in the inversion, as shown in Figures 16b and 17b, naturally improves the fit to the overtones but also greatly reduces the range of acceptable models in the crust. This is most dramatic for the Tibetan inversion in which the range of allowed crustal shear velocities and crustal thicknesses is much narrower than if only fundamental mode data are applied.

These results imply that the inclusion of higher-mode observations in inversions for crustal structure significantly improves the crustal part of the model, which is otherwise hard to constrain. In addition, by narrowing the range of admissible crustal models, it also improves the mantle part of the model. It can be seen in Figures 16b and 17b that the range of mantle models also narrows when crustal overtone data are introduced in the inversion. This is not because the overtone data constraint the mantle, however. It is because the range of admissible crustal models has been reduced and the trade-off between crustal and mantle structures has been ameliorated.

6. Conclusions

We have shown that when reliable measurements of higher crustal modes can be obtained in sufficient number to justify the construction of dispersion maps, they provide valuable information to reduce the range of admissible models of crustal velocities and thickness and help to resolve the trade-off between crustal and mantle structures thereby improving

uppermost mantle structures as well. We argue that the first higher mode between about 8 sec and 18 sec period is the principal target for reliable travel time estimates. It is best excited by events deeper than the shallow crust and propagates most efficiently in continental regions where crust is thick. For these reasons, we sought measurements of the first higher mode Rayleigh and Love waves in Central Asia and obtained a data set of measurements for about 500 paths across the region. Tomographic maps of the group velocity of the first higher modes provide new information about crustal structure across much of Central and Southern Asia and part of the Middle East. Monte Carlo inversion of first higher-mode and fundamental mode dispersion at several locations show that the higher modes significantly reduce the range of acceptable crustal models and improve the vertical resolution of the crust from the mantle. Further development of the higher-mode data set will permit a general 3-D simultaneous inversion for shear velocity structure of the crust and upper mantle in this region with better vertical resolution than in our existing model (Shapiro and Ritzwoller, 2002).

Although the application of higher modes provides powerful constraints on crustal structure, the method is probably not generally applicable. The reason is that even in Central Asia the number of reliable higher mode measurements is about thirty times smaller than reliable fundamental mode observations made on the same seismic recordings. This difference is largely attributable to the fact that the higher modes are excited less efficiently by shallow crustal events and, for a given depth of sensitivity, the overtones are at a higher frequency and therefore scatter more strongly from crustal inhomogeneities than fundamental modes. For these reasons, higher modes are typically poorly observed. In fact, the 1:30 ratio of overtone to fundamental mode measurements that we observed is anomalously large relative to the rest of the world because of the thick Central Asian crust. This method will probably not be feasible in continental regions with normal crustal thickness that are devoid of deep crustal seismicity.

Acknowledgements

We gratefully acknowledge the staffs at the IRIS-DMC and the GEOSCOPE data center for providing the waveform data on which the higher mode measurements were obtained. We are also particularly grateful to Anne Sheehan and Francis Wu for providing waveform data obtained from the HIMNT PASSCAL Experiment in Nepal prior to the general release of these data. All maps were generated with the Generic Mapping Tools (GMT) data processing and display package (Wessel & Smith, 1991, 1995). This work was supported by NSF grant EAR-0337622.

References

Alexander, S.S., 1962. A Study of the Normal Modes of Surface Waves Across the Western United States, *J. geophys. Res.*, **67**, 3537-3538.

Barmin, M.P., Levshin, A.L., & Ritzwoller M.H., 2001. A fast and reliable method for surface wave tomography, *Pure Appl. Geophys.*, **158**, 1351-1375.

Bourjot, L. & Romanowicz, B., 1992. Crust and upper mantle tomography in Tibet using surface waves, *Geophys. Res. Lett.*, **19**, 881-884.

Brune, J. & Dorman, J., 1963. Seismic waves and Earth structure in the Canadian shield, *Bull. seismol. Soc. Am.*, **53**, 167 - 210.

Crampin S., 1964. Higher modes of seismic surface waves: preliminary observations, *Geophys. J. R. astr. Soc.*, **9**, 35 -37.

Crampin, S., 1966a. Higher modes of seismic surface waves: propagation in Eurasia, *Bull. seism. Soc. Am.*, **56**, 1227 - 1239.

Crampin, S., 1966b. Higher-mode seismic surface waves from atmospheric nuclear explosions over Novaya Zemlya, *J. geophys. Res.*, **71**, 2951-2958.

Crampin, S. & King, D., 1977. Evidence for anisotropy in the upper mantle beneath Eurasia from the polarization of higher mode seismic surface waves, *Geophys. J. R. astr. Soc.*, **49**, 59-85.

Curtis, A. & Woodhouse, J.H., 1997. Crust and upper mantle structure beneath the Tibetan plateau and surrounding regions from interevent surface wave inversion, *J. geophys. Res.*, **102**, 11,789-11,813.

Ekström, G., Tromp, J., & Larson, E.W.F., 1997. Measurements and global models of surface waves propagation, *J. geophys. Res.*, **102**, 8137-8157.

Ewing W.M., Jardetzky, W.S., & Press F., 1957. *Elastic waves in layered media*, McGraw-Hill Book Co.

Friederich W., 2003. The S-velocity structure of the East Asian mantle from inversion of shear and surface wave forms. *Geophys. J. Int.*, **153**, 88-102.

Gabriels, P., Snieder R., & G. Nolet, 1987. In situ measurements of shear velocity in sediments with higher mode Rayleigh waves, *Geophys. Prosp.*, **35**, 187-196, 1987

Griot, D.-A., Montagner, J.-P., & P. Tapponnier, 1998. Phase velocity structure from Rayleigh and Love waves in Tibet and its neighboring regions, *J. geophys. Res.*, **103**, 21,215- 21,232.

Huang, Z., Su, W., Peng, Y., Zheng, Y., & Li, H., 2003. Rayleigh wave tomography of China and adjacent regions, *J. geophys. Res.*, **108**, 2073, doi:10,1029/2001JB001696.

Kovach R.L. & Anderson, D.L., 1964. Higher mode surface waves and their bearing on the structure of the earth's mantle, *Bull. seismol. Soc. Am.*, **54**, 161 -182.

Lebedev, S. & Nolet, G., 2003. Upper mantle beneath Southeast Asia from S velocity tomography, *J. geophys. Res.*, **108**, doi:10.1029/2000JB000073.

Levshin, A.L., Pisarenko, V.F., & Pogrebinsky, G.A., 1972a. On a frequency-time analysis of oscillations. *Ann. Geophys.*, **28**, 211-218.

Levshin, A.L., Frantsuzova, V.I., & Shkadinskaya, G.V., 1972b. Higher modes of Rayleigh waves and upper mantle structure. In *Comput. Seismology*, (ed. Keilis-Borok V.I.), Consult. Bureau, N.Y. - London, 93-100.

Levshin, A.L., Yanovskaya, T.B., Lander, A.V., Bukchin, B.G., Barmin, M.P., Ratnikova, L.I., & Its, E.N., 1989. *Seismic Surface Waves in Laterally Inhomogeneous Earth.* (Ed. V. I. Keilis-Borok), Kluwer Publ. House, Dordrecht/ Boston/ London.

Levshin, A.L., Ratnikova, L.I., & Berger, J., 1992. Peculiarities of surface wave propagation across the Central Eurasia. *Bull.seism. Soc. Am.*, **82**, 2464-2493.

Nolet, G., 1975. Higher Rayleigh modes in Western Europe, *Geophys. Res. Lett.*, **2**, 60-62.

Nolet, G., 1977. The upper mantle under Western Europe inferred from the dispersion of Rayleigh modes, *J. Geophysics*, **43**, 265-285.

Nolet, G., 1978. Simultaneous inversion of seismic data, *Geophys. J. Roy. astr. Soc.*, **55**, 679-691.

Nolet, G., 1987. Waveform Tomography, in: *Seismic Tomography*, G. Nolet (ed.), Reidel, Dordrecht, 301-322.

Officer, C.B., 1958. *Introduction to the theory of sound transmission*, McGraw-Hill Co., N.Y.

Oliver, J., 1962. A summary of observed surface wave dispersion. *Bull. seismol. Soc. Am.*, **52**, 81-86.

Oliver J., J. Dorman, and G. Sutton, 1959. The second shear mode of continental Rayleigh waves. *Bull. seismol. Soc. Am.*, **49**, 379 -389.

Oliver J. and M. Ewing, 1957. Higher modes of continental Rayleigh waves. *Bull. seismol. Soc. Am.*, **47**, 187-204.

Oliver J. and M. Ewing, 1958. Normal modes of continental Rayleigh waves. *Bull. seismol. Soc. Am.*, **48**, 33-49.

Owens, T.J., Randall, G.E., Wu, F.T., & Zeng, R.S., 1993. PASSCAL Instrument performance during the Tibetan Plateau passive seismic experiment, *Bull. seismol. Soc. Am.*, **83**, 1959-1970.

Ritzwoller, M.H. & Levshin, A.L., 1998. Surface wave tomography of Eurasia: group velocities, *J. geophys. Res.*, **103**, 4839-4878.

Ritzwoller, M.H. & Levshin, A.L., 2002. Estimating shallow shear velocities with marine multi-component seismic data, *Geophysics*, **67**, 1991-2004.

Ritzwoller, M.H., Levshin, A.L., Ratnikova, L.I., & Egorkin, A.A., 1998. Intermediate period group velocity maps across Central Asia, Western China, and parts of the Middle East, *Geophys. J. Int.*, **134**, 315-328.

Ritzwoller, M.H., Shapiro, N.M., Barmin, M.P., & Levshin, A.L., 2002, Global surface wave diffraction tomography, J. geophys. Res., **107** , B12,2335,doi:10.1029/2002JB001777,2002

Shapiro, N.M. & Ritzwoller, M.H., 2002. Monte-Carlo inversion for a global shear velocity model of the crust and upper mantle, *Geophys. J. Int.*, **151**, 88-105.

Shapiro, N.M., Ritzwoller, M.H., Molnar, P., & Levin, V., 2004. Thinning and flow of Tibetan crust constrained by seismic anisotropy, Science, submitted.

Sheehan, A.F., Wu, F.T., Blume, F., Monsalve, G., Gilbert, H., de la Torre, T., Bendick, R., Schulte-Pelkum, V., Bilham, R., Huang, G.C., Pandey, M.R., & Liu, H.B., 2002. Himalayan Nepal Tibet broadband seismic experiment (HIMNT), *Eos Trans.*, **83**, Am. Geophys. Union, Fall Meet. Suppl., Abstract S61D-11.

Trampert, J. & Woodhouse, J.H., 1995. Global phase velocity maps of Love and Rayleigh waves between 40 and 150 s period, *Geophys. J. Int.*, **122**, 675-690.

van Heijst, H.J. & Woodhouse, J.H., 1999. Global high-resolution phase velocity distribution of overtone and fundamental-model surface waves determined by mode branch stripping, *Geophys. J. Int.*, **137**, 601-620.

Wessel, P. & Smith, W.H.F., 1991. Free software helps map and display data. *Eos Trans.*, AGU, **72**, 441.

Wessel, P. & Smith, W.H.F., 1995. New version of the Generic Mapping Tools released, Eos Trans. AGU, 76, 329.

Woodhouse, J.H., 1988. The calculation of the eigenfrequencies and eigenfunctions of the free oscillations of the Earth and the Sun, in: *Seismological Algorithms* (D. J. Doornbos, ed.), 321-370.

Wu, F.T. & Levshin, A.L., 1994. Surface wave tomography of China using surface waves at CDSN. *Phys. Earth Planet Inter.*, **84**, 59-77.

Wu, F.T., Levshin, A.L., & Kozhevnikov, V.M., 1997. Rayleigh Wave Group Velocity Tomography of Siberia, China and the Vicinity. *Pure and Appl. Geophysics*, **149**, 447-473.

Yoshizawa K. & Kennett B.L.N, 2002. Non-linear waveform inversion for surface waves with a neighborhood algorithm - application to multimode dispersion measurements, *Geophys. J. Int.*, **149**, 118-133.

Table 1. RMS-Misfit of Dispersion Maps to Measurements.

Wave	*Period (s)*	*Initial Res. (s)*	*Final Res. (s)*	*Var. Red. (%)*
Rayleigh	10	28.8	19.6	54
Rayleigh	12	24.2	18.5	42
Rayleigh	14	27.4	19.1	51
Rayleigh	17	28.6	20.3	50
Love	10	29.2	18.9	58
Love	12	29.6	19.7	56
Love	14	31.8	17.6	69
Love	17	34.6	19.9	67

Figure Captions

Figure 1. Multiple reflection of shear waves in a homogeneous crust as the physical basis for crustal overtones. The incidence angle $i > i_{crit}$.

Figure 2. Shear velocity profiles for a variety of locations in Central Asia taken from the 3-D model of Shapiro and Ritzwoller (2002).

Figure 3. Group velocity curves at a point within the Kazakh Platform (same location as the vertical profile shown in Figure 2 taken from Shapiro and Ritzwoller, 2002), computed using the method of Woodhouse (1988). (a) Rayleigh waves for the fundamental mode (R_0), and the first through fourth higher modes ($R_1 - R_4$). (b) Love waves for the fundamental mode (L_0), and the first through fourth higher modes ($L_1 - L_4$).

Figure 4. Phase (top) and group (bottom) velocity dispersion curves for the first Rayleigh higher mode for the different geographical locations identified in Figure 2.

Figure 5. Radial sensitivity kernels to shear velocity for the first Rayleigh higher mode computed for a model of the Tibetan plateau (shown in Figure 2) at the three indicated periods: (a) phase velocity kernels and (b) group velocity kernels.

Figure 6. Modal quality factor, Q^*, as a function of period for the fundamental (R_0) and the first higher Rayleigh (R_2) modes for the Kazakh Platform and the Tibetan plateau. Crustal and mantle structure are shown in Figure 2 and the intrinsic Q model is 600 in the crust, and reduces similarly in both regions in the mantle.

Figure 7. Radiation patterns of the fundamental (R_0) and first higher (R_1) Rayleigh modes for the Tibetan plateau model (Fig. 2) at periods from 8 sec to 16 sec. Source depths and the source mechanism are indicated. Higher mode radiation patterns are more likely to display four lobes than the fundamental mode radiation patterns.

Figure 8. Dependence of the spectral amplitudes of the fundamental and first higher Rayleigh modes on source depth: (a) Tibetan plateau model and (b) Kazakh Plat-

form model from Figure 2. Solid lines represent the amplitudes of the fundamental mode (R_0) and dashed lines are the first higher mode (R_1).

Figure 9. Synthetic seismograms of the vertical component of the fundamental (L_0, R_0) and first higher (L_1, R_1) Rayleigh (a) and Love (b) modes for the Tibetan model (Fig. 2) and source depths as indicated. The epicentral distance is 2000 km and the relative magnification of the seismograms increases by a factor of 1.5 with each depth increment. The source mechanism is shown in Figure 8.

Figure 10. Frequency-time (FTAN) diagram for an event in N. Pakistan on May 10, 1992 (depth 33 km, M_s= 5.6) recorded at BUDO (Tibetan Plateau PASSCAL Experiment, 1991-1992, Owens et al., 1993). Epicentral distance is 1890 km. Left: raw FTAN diagram. Right: FTAN diagram for the extracted higher mode.

Figure 11. Same as Figure 10, but for an event in the Hindu Kush on October 27, 2001 (depth 96 km, m_b=4.8) recorded at HILE (HIMNT PASSCAL Experiment, 2000-2001, Sheehan et al., 2003). Epicentral distance 1880 km.

Figure 12. Number of paths for the higher mode measurements as a function of period. Rayleigh - solid line; Love - dashed line.

Figure 13. Path density for the first higher mode at the indicated periods: Rayleigh mode (left side) and Love mode (right side). Path density is presented as the number of paths crossing each $2^\circ \times 2^\circ$ cell.

Figure 14. Group velocity maps for the first higher modes at the indicated periods: (left) Rayleigh mode and (right) Love mode.

Figure 15. Differential group velocity maps for the first higher modes (observed - predicted) at the indicated periods:(left) Rayleigh mode and (right) Love mode.

Figure 16. Example of the results of a Monte-Carlo inversion of observed data for a shear velocity profile beneath the Northern Tien-Shan (42°N, 74°E). Left panels display the

observed curves as solid (Rayleigh) and dashed (Love) black lines. Rayleigh and Love wave fundamental mode group (U_0) and phase (C_0) velocities are shown together with Rayleigh and Love wave first higher-mode group velocities (U_1). Gray dispersion curves are computed from the range of models shown in the right panel. Right panels display the range of models that fit the data. (a, Top Row) Only fundamental mode data are used in the inversion. (b, Bottom Row) Both fundamental and overtone data are jointly used in the inversion. The joint inversion reduces the range of acceptable models in both the crust and the mantle and reduces the range of crustal thicknesses while fitting all data acceptably.

Figure 17. Same as Figure 16, but for a location in South-Western China (30°N, 100°E).

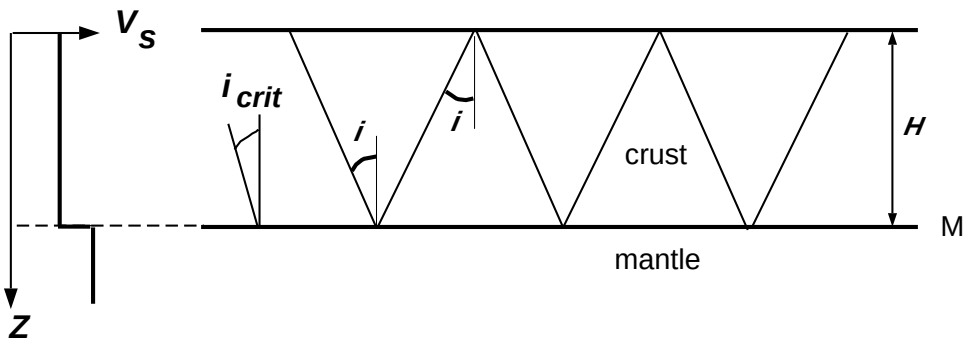

Figure 1:

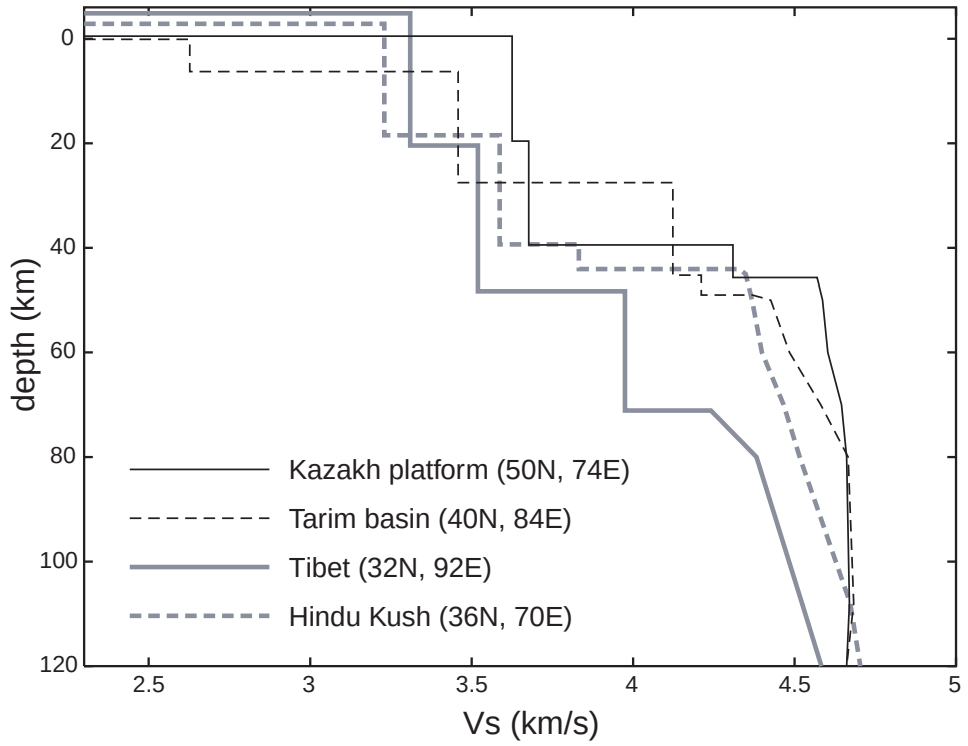

Figure 2:

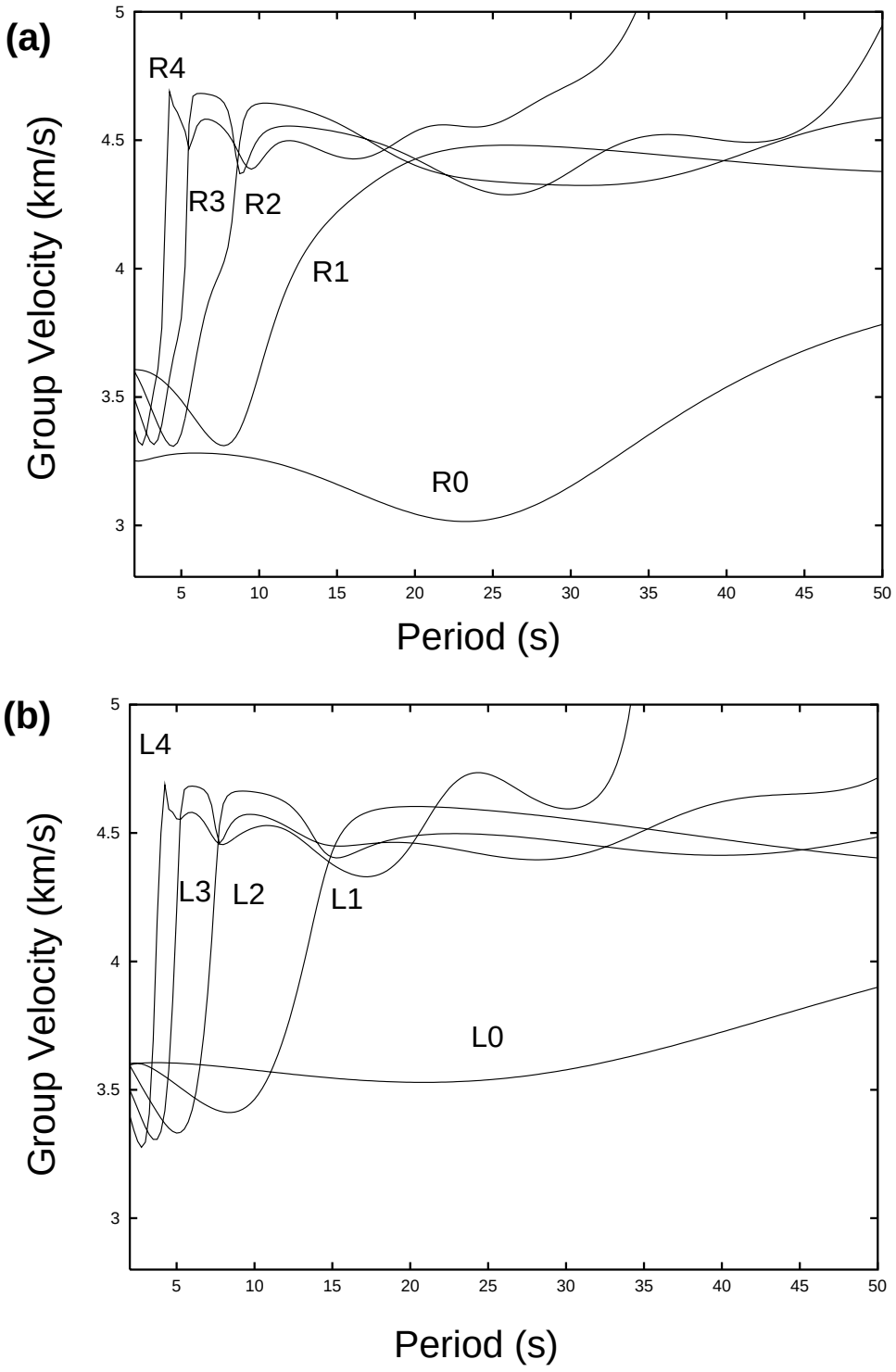
(a)
R4
R3
R2
R1
R0
Group Velocity (km/s)
Period (s)
(b)
L4
L3
L2
L1
L0
Group Velocity (km/s)
Period (s)

Figure 3:

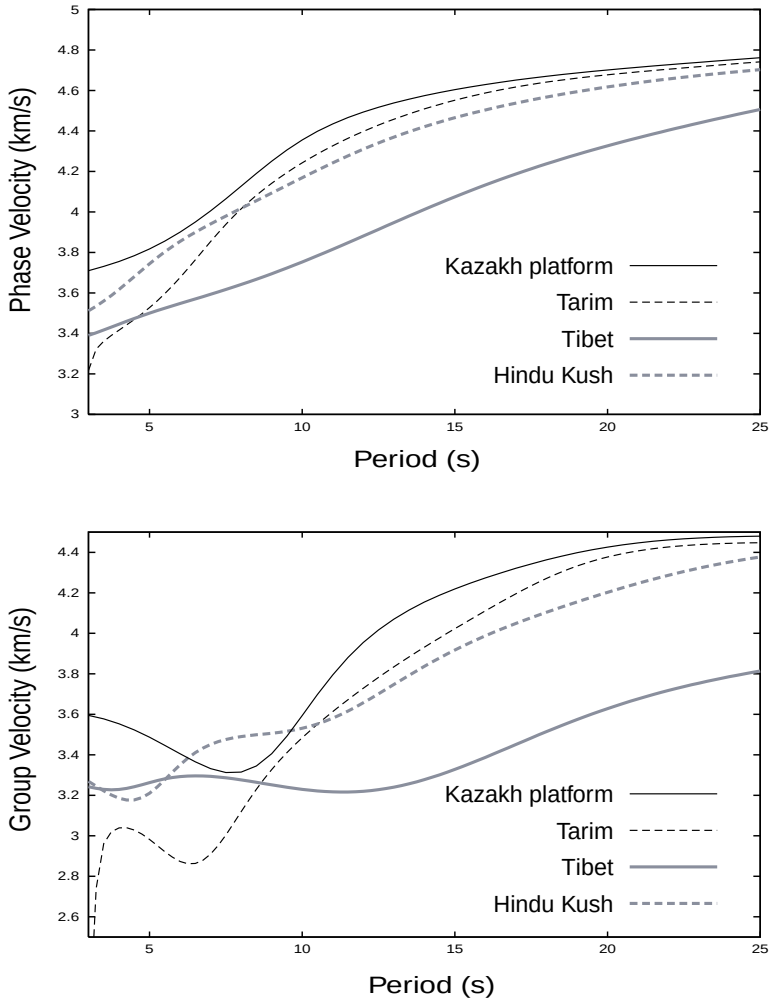
Phase Velocity (km/s)
Period (s)
Kazakh platform
Tarim
Tibet
Hindu Kush
Group Velocity (km/s)
Period (s)
Kazakh platform
Tarim
Tibet
Hindu Kush

Figure 4:

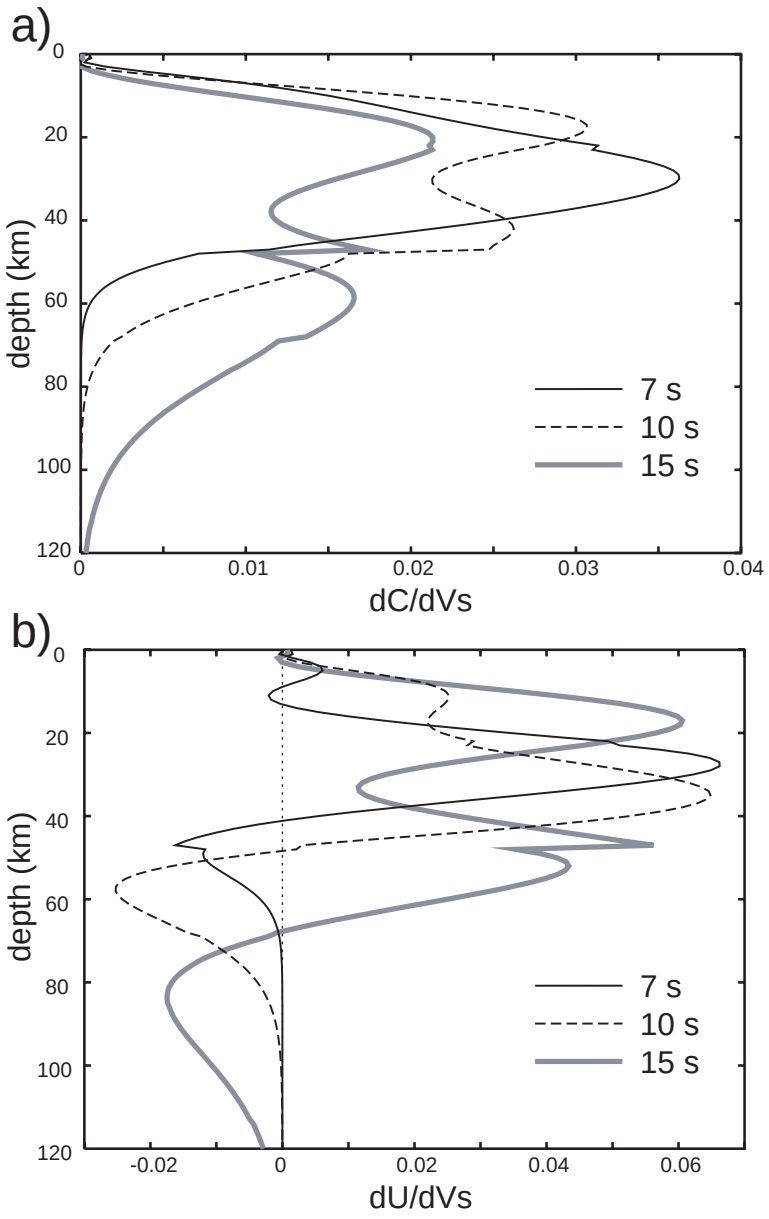
a)
b)
depth (km)
dC/dVs
dU/dVs
7 s
10 s
15 s
0
20
40
60
80
100
120
0.01
0.02
0.03
0.04
-0.02
0.06

Figure 5:

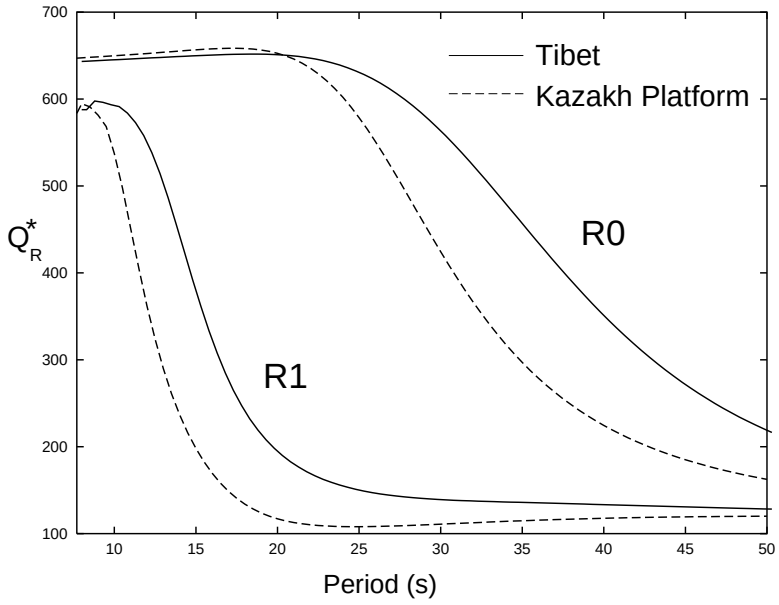
Tibet
Kazakh Platform
R0
R1
Q^*_R
Period (s)
700
600
500
400
300
200
100
10
15
20
25
30
35
40
45
50

Figure 6:

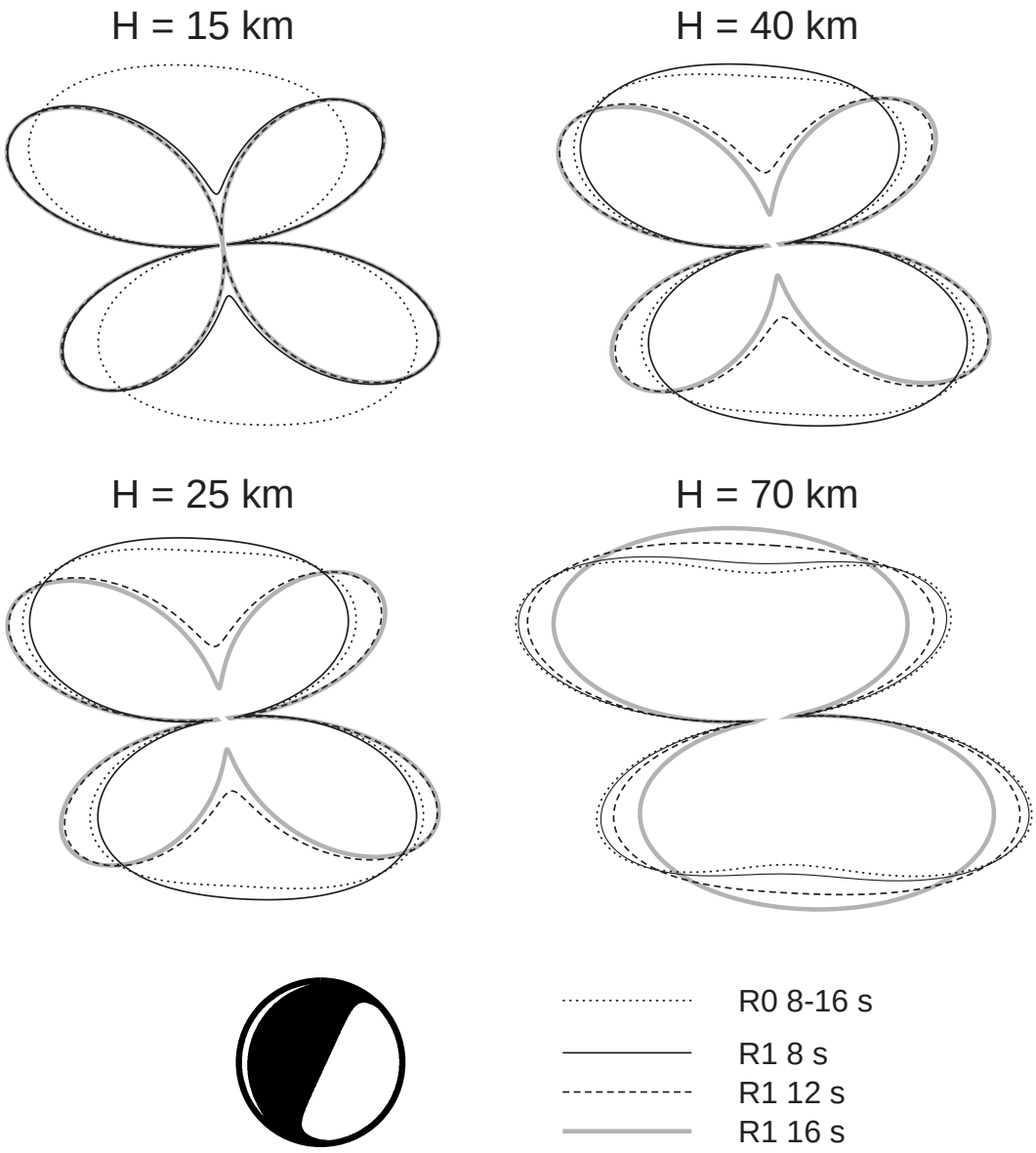

Figure 7:

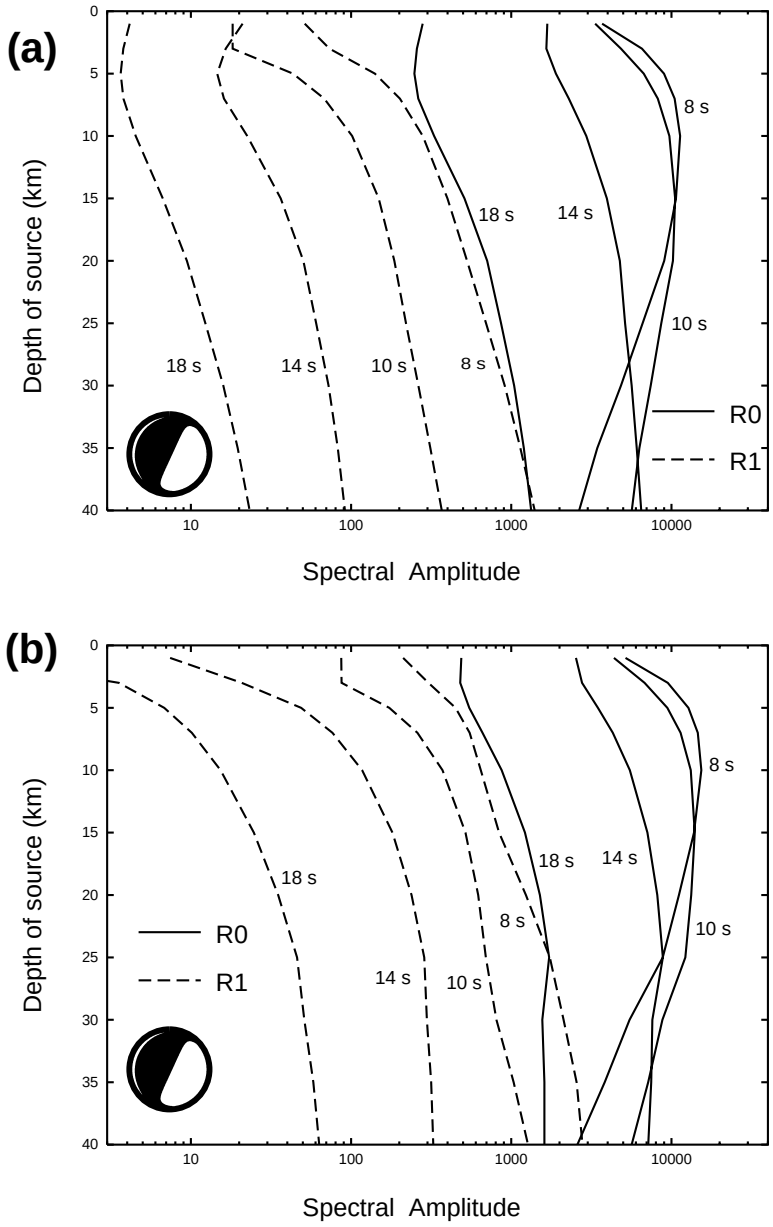
(a)
Depth of source (km)
Spectral Amplitude
18 s
14 s
10 s
8 s
R0
R1
(b)
Depth of source (km)
Spectral Amplitude
18 s
14 s
10 s
8 s
R0
R1

Figure 8:

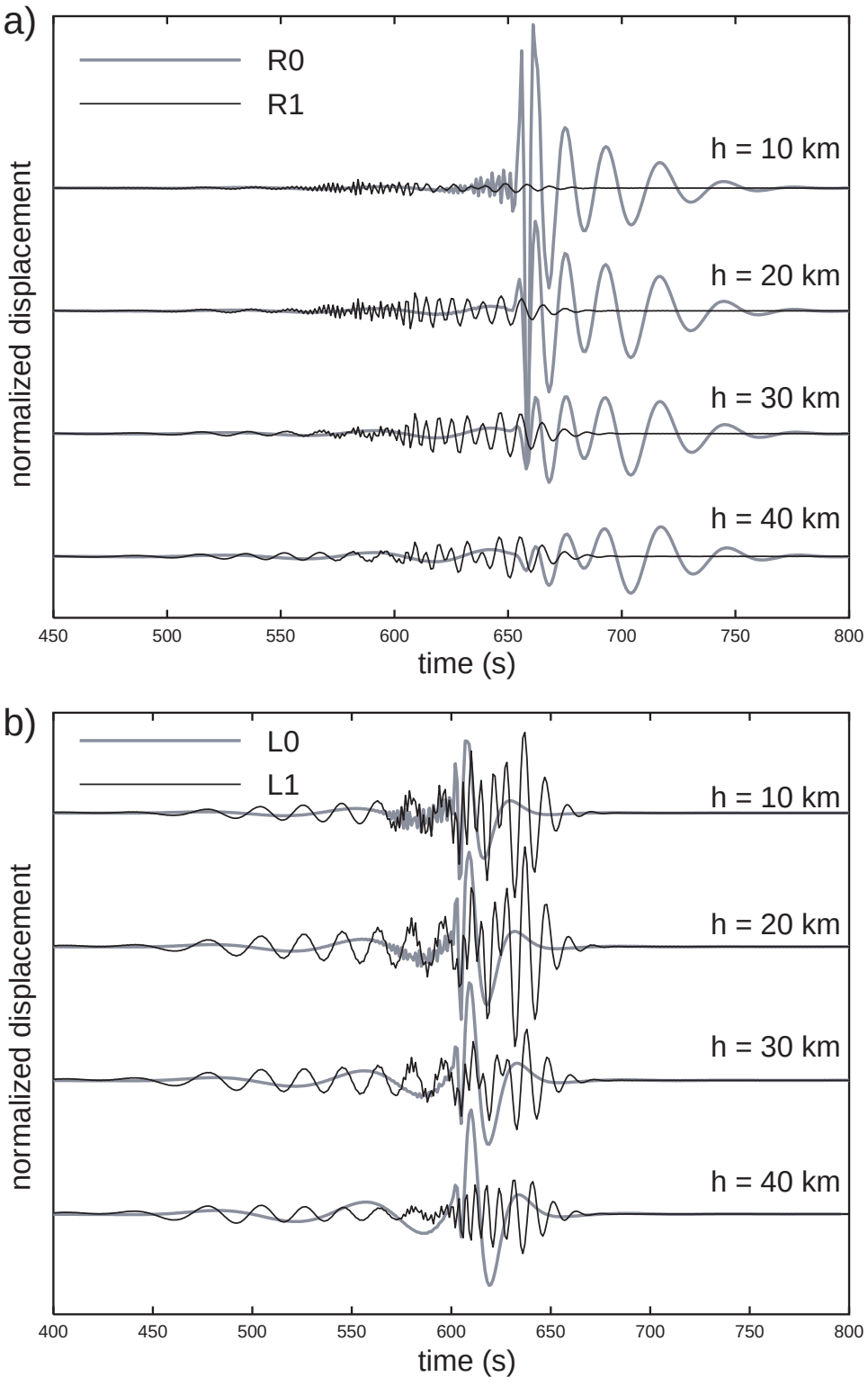
a)
R0
R1
h = 10 km
h = 20 km
h = 30 km
h = 40 km
normalized displacement
450
500
550
600
650
700
750
800
time (s)
b)
L0
L1
h = 10 km
h = 20 km
h = 30 km
h = 40 km
normalized displacement
400
450
500
550
600
650
700
750
800
time (s)

Figure 9:

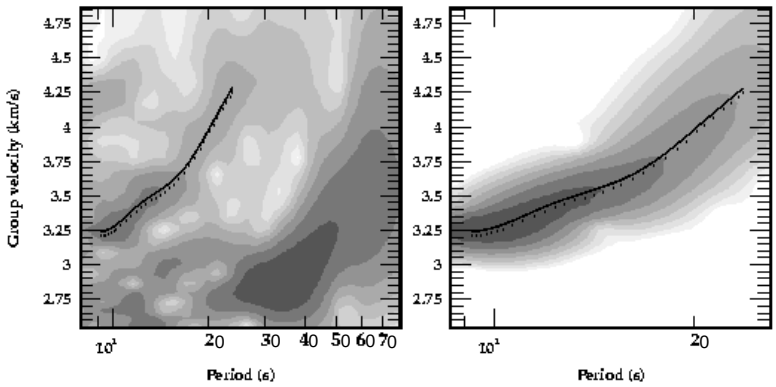

Figure 10:

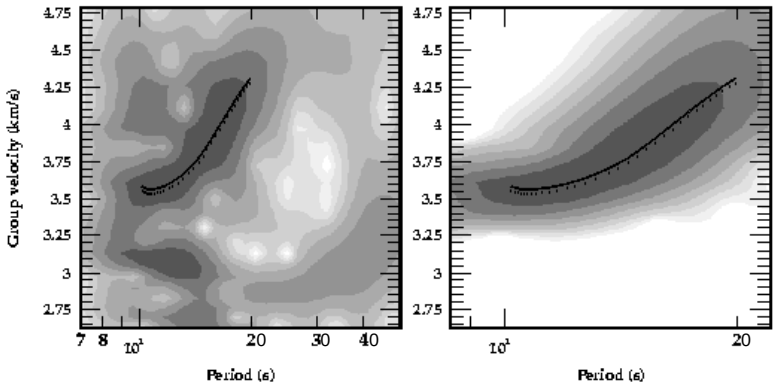

Figure 11:

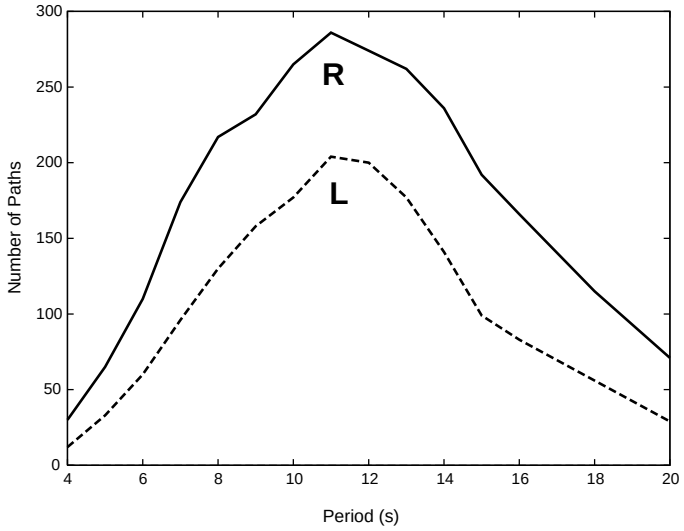

Figure 12:

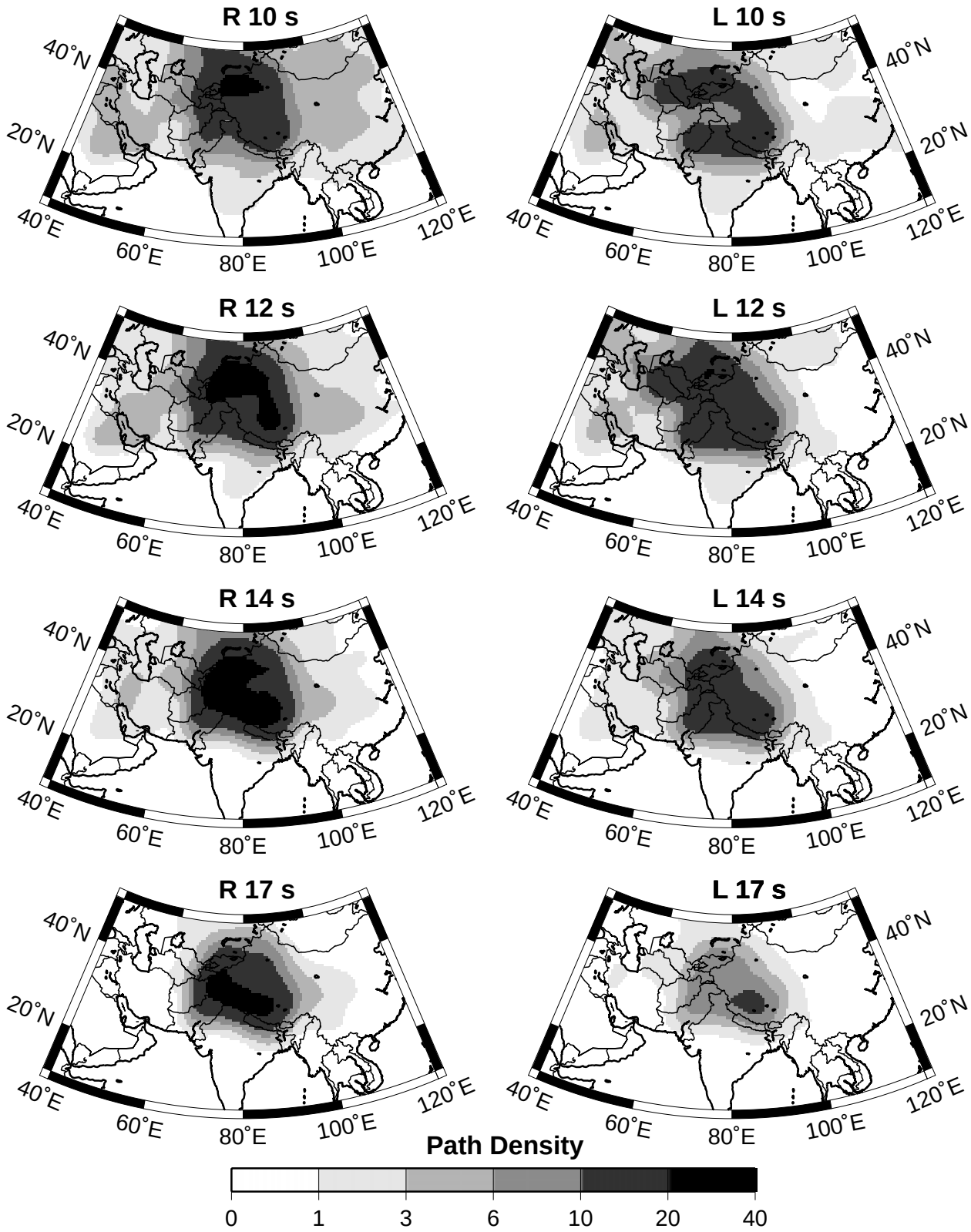
R 10 s
L 10 s
R 12 s
L 12 s
R 14 s
L 14 s
R 17 s
L 17 s
40˚N
20˚N
40˚E
60˚E
80˚E
100˚E
120˚E
Path Density
0
1
3
6
10
20
40

Figure 13:

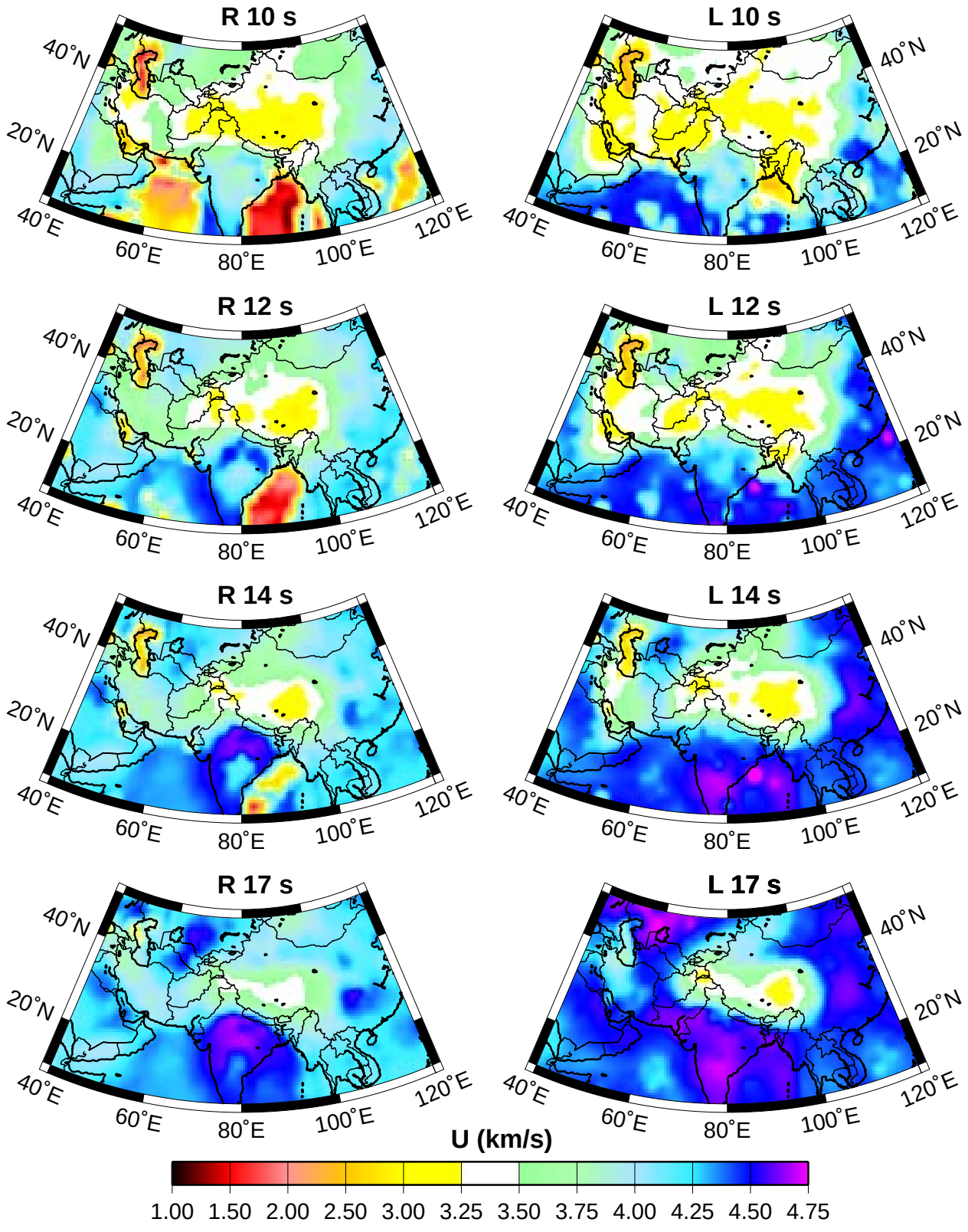
R 10 s
L 10 s
R 12 s
L 12 s
R 14 s
L 14 s
R 17 s
L 17 s
40°N
20°N
40°E
60°E
80°E
100°E
120°E
U (km/s)
1.00 1.50 2.00 2.50 3.00 3.25 3.50 3.75 4.00 4.25 4.50 4.75

Figure 14:

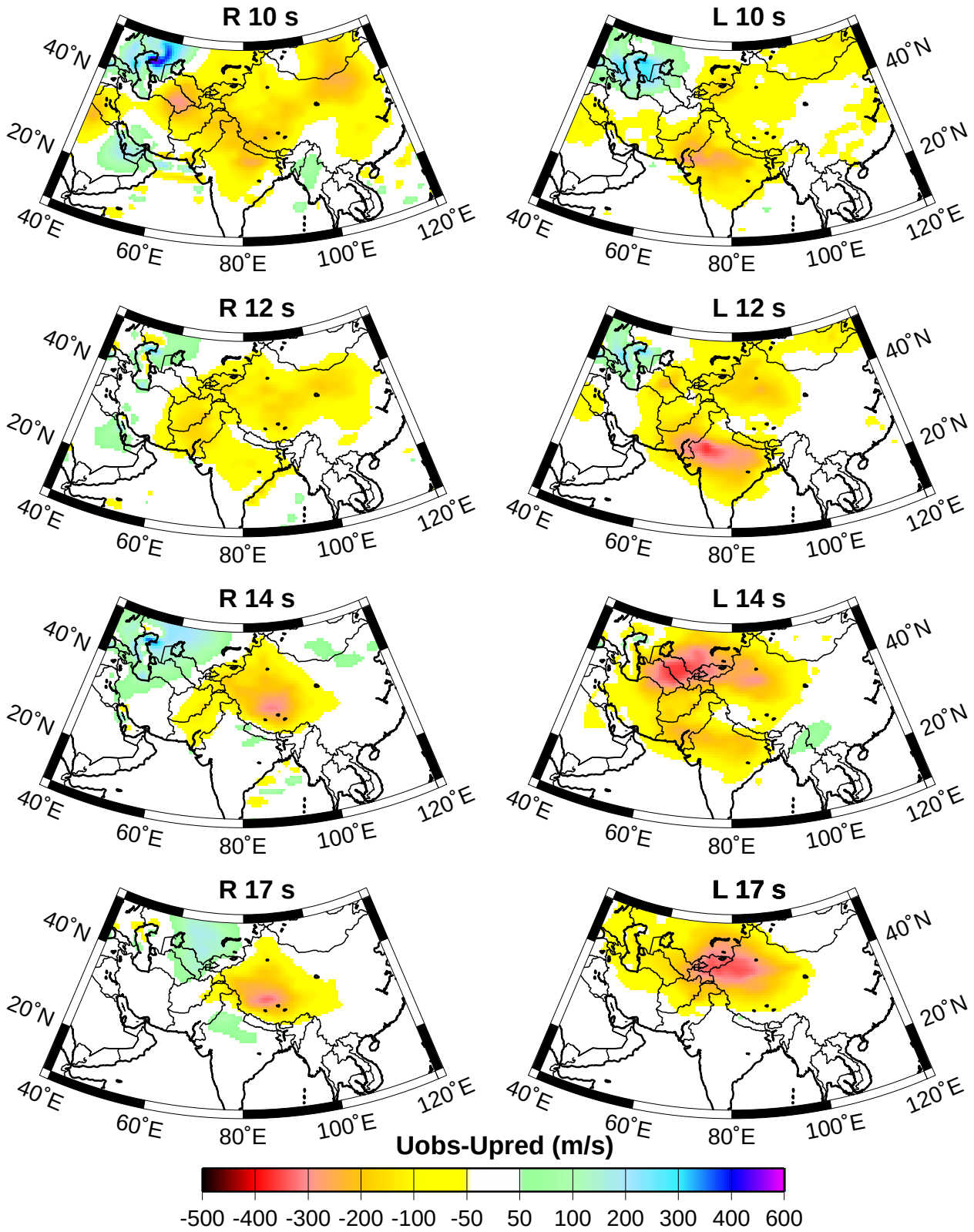
R 10 s
L 10 s
R 12 s
L 12 s
R 14 s
L 14 s
R 17 s
L 17 s
40°N
20°N
40°E
60°E
80°E
100°E
120°E
Uobs-Upred (m/s)
-500 -400 -300 -200 -100 -50 50 100 200 300 400 600

Figure 15:

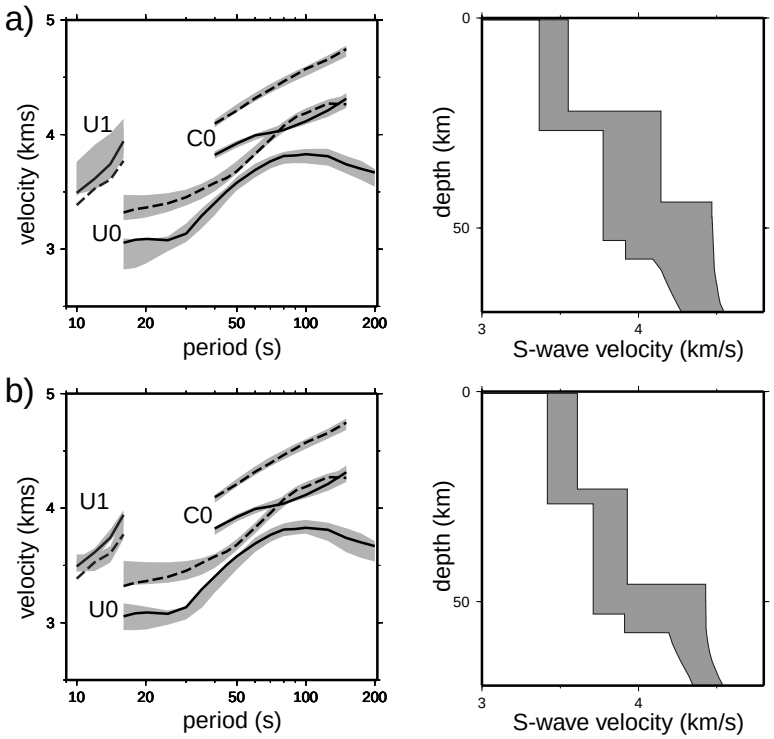

Figure 16:

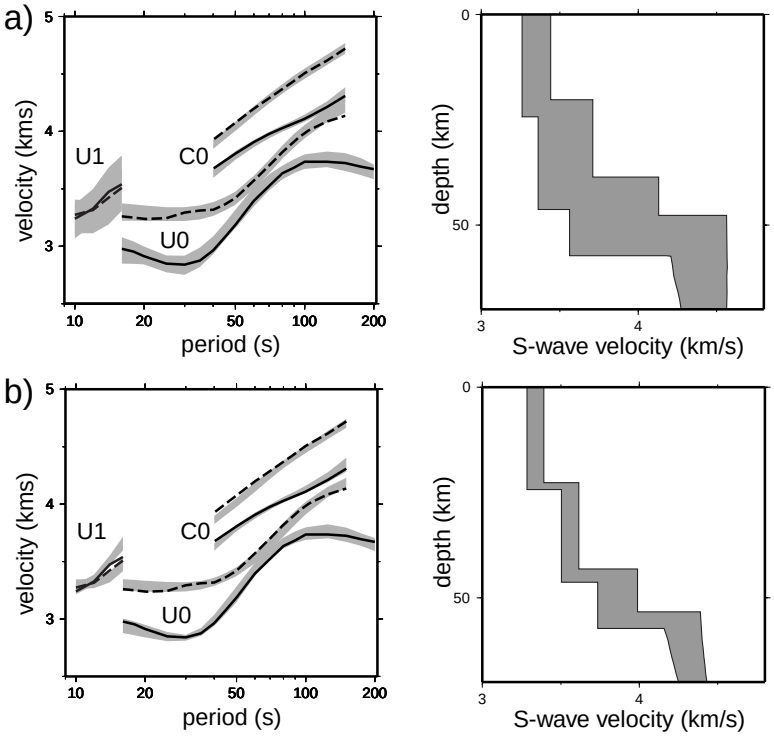

Figure 17: